aerospace

MDPI

Article

Fuelless On-Orbit Assembly of a Large Space Truss Structure Using Repulsion of the Service Spacecraft by Robotic Manipulators

Vladislav Orlov, Uliana Monakhova, Mikhail Ovchinnikov and Danil Ivanov *

Keldysh Institute of Applied Mathematics, Russian Academy of Sciences, 125047 Moscow, Russia; orlov.vv@phystech.edu (V.O.); monakhova@phystech.edu (U.M.); ovchinni@keldysh.ru (M.O.)
* Correspondence: danilivanovs@gmail.com

Abstract: A servicing spacecraft motion control approach for the problem of on-orbit truss structure assembly is developed in this paper. It is considered that a cargo container with a rod set and servicing spacecraft are in orbit initially. The assembly procedure is based on spacecraft free-flight motion between the structure's specified points. The spacecraft is equipped with two robotic manipulators capable of attaching to the structure and holding rods. In addition, the spacecraft can repulse from the structure with a given relative velocity using a manipulator, so the spacecraft and the structure receive impulses. The repulsion velocity vector is calculated in order to reach the structure target point to deliver and install the rod into the truss structure, or to reach the cargo container and take a rod. The problem of searching the repulsion velocity is formulated as an optimization problem with constraints, taking into account the limited value of the repulsion velocity, collision avoidance with structure, restrictions on the angular velocity and translational motion of the structure in the orbital reference frame. This problem is solved numerically with an initial guess vector obtained analytically for simplified motion cases. The application of the proposed control scheme to the assembly of a truss-based antenna is demonstrated. It is shown that the servicing spacecraft is successfully transferred between the structure points by means of manipulator repulsion. Main features and limitations of the assembly problem using a spacecraft with two manipulators are discussed.

Keywords: on-orbit assembly; formation flying; truss structure; motion control; numerical simulation; optimization

Citation: Orlov, V.; Monakhova, U.; Ovchinnikov, M.; Ivanov, D. Fuelless On-Orbit Assembly of a Large Space Truss Structure Using Repulsion of the Service Spacecraft by Robotic Manipulators. *Aerospace* **2024**, *11*, 635. https://doi.org/10.3390/aerospace11080635

Academic Editor: Gabriella Gaias

Received: 4 July 2024
Revised: 29 July 2024
Accepted: 31 July 2024
Published: 2 August 2024

1. Introduction

An application of on-orbit assembly for new space systems is expected to become a trend. It allows building large structures in near-Earth orbit to improve the characteristics of scientific, communication, or observation missions. The size of the on-Earth assembled space structure is limited by the dimensions of the launcher payload volume, so many modern spacecrafts enlarge their size by deployable elements. However, any joints are greatly affected by launch vibrations and, after the launch, they can be out of order in orbit. These problems can be overcome by large structure on-orbit assembly; a current state-of-the-art in this field is analyzed in [1]. The space structure components can be delivered to the orbit by several launches and then assembled, increasing the overall size of the resulting space object. An additional advantage discussed in [2] is that the on-orbit assembled orbital structure is not exposed to on-the-ground conditions such as the on-Earth gravitational stress effect and air/oxygen influence on the structure materials.

Telescope or reflector mirrors are not limited in dimensions if their modules are transferred into orbit using several launch vehicles. This concept makes many project planning tasks feasible, as discussed in [3]. Furthermore, some new mission ideas such as telescope reflector elements acting as a solar sail [4] are being developed. As discussed in [1], deploying strategies should be classified based on economic advantage. Different strategies are presented in [5] and evaluated economically in [6]. One of the approaches of on-orbit

assembly considers modules capable of docking that are placed by the launchers in close orbits [7,8]. For example, paper [9] proposes a space telescope that can be reconfigured, consisting of two 3U CubeSats capable of autonomous docking, undocking, and re-docking with a small central "15U" class microsatellite. Another approach of on-orbit assembly considers modules to be transferred from cargo container (CC) to the target position of the structure to be assembled [3]. In paper [10], a space solar power plant assembled by such an approach is proposed. The first approach implies onboard propulsion in order to control modules orbital motion, while the CC-based on-orbit assembly approach could rely on fuelless module motion control methods, such as using methods installed on the CC manipulators. The assembling space structure can be truss-based as for the OSAM-2 Mission [11], which involves the on-orbit 3D printing of a lattice truss to deploy solar cells on it. Another method to transfer modules or rods of the truss structure from the CC to the target position is to use a servicing spacecraft (SS). A review on the variety of SS applications is provided in [12].

The problem of the SS's autonomous control is one of the most challenging in space-flight dynamics, since it usually implies docking to space objects. In the case of active space debris removal missions, the SS's relative motion control is aimed at docking to non-cooperative tumbling objects as in [13], which requires taking into account the object chaotic attitude motion. One of the approaches considered in the literature is to use robotic manipulators to perform the docking. The dynamics of spacecraft manipulators for the on-orbit assembly problem have been sufficiently investigated in many papers, particularly in [14–19]. So, in this paper, the problem of manipulator control is not considered; it is assumed that this separate task can be solved. A small SS for the on-orbit assembly is considered due to the trend of spacecraft miniaturization for modern space missions. Miniature manipulators [20,21], gas thrusters, and ion thrusters [22,23] are now available for CubeSat-type satellites, providing the necessary element basis for SS's motion control. Several CubeSat-based in-orbit servicing missions are under development nowadays, for example, the SpEye mission for the demonstration of proximity operations capabilities of a nanosatellite [24].

This paper presents a new approach for SS's motion control in the problem of truss structure (TS) assembly. The proposed approach is based on the use of manipulators for repulsion and catching, so the motion of SSs between TS points can be considered as free flight. The main advantage of this approach is that it does not require an onboard propulsion system to perform the SS's transfers; the on-orbit assembly requires renewable energy with solar panels' electrical power for repulsion and catching by manipulators. The proposed approach takes into account collision avoidance with the TS during the free flight. The SS transfer problem can be considered as boundary problem with restrictions, as in paper [25]. Two numerical search algorithms to solve this problem were applied. Since these algorithms are sensitive to the initial guess vector, simplified motion cases were considered, allowing to analytically calculate the repulsion velocity vector required for transfer.

The rest of the paper has the following structure. In Section 2, the problem statement and main assumptions are formulated. In Section 3, translational and attitude motion equations used in the paper are presented. In order to solve the SS transfer problem, the change in initial conditions due to repulsion is analytically derived in Section 4. The solution of the boundary problem for the planar motion case is provided in Section 5. For the spatial motion case, this problem is to be solved only numerically; two search algorithms are described in Section 6. Furthermore, finally, in Section 7, a demonstration example of antenna-like truss structure assembly is shown.

2. Problem Statement

The objects considered in this paper are the following: a CC with a set of rods, an installing platform placed on the CC, a TS to be assembled using rods and an SS with two manipulators. It is assumed that, using manipulators, the SS is capable of repelling from

the CC or TS with the required velocity and to move relative to the structure during the free flight. Another function of the manipulator is to hold one rod and fix it to the TS. These objects are presented in Figure 1.

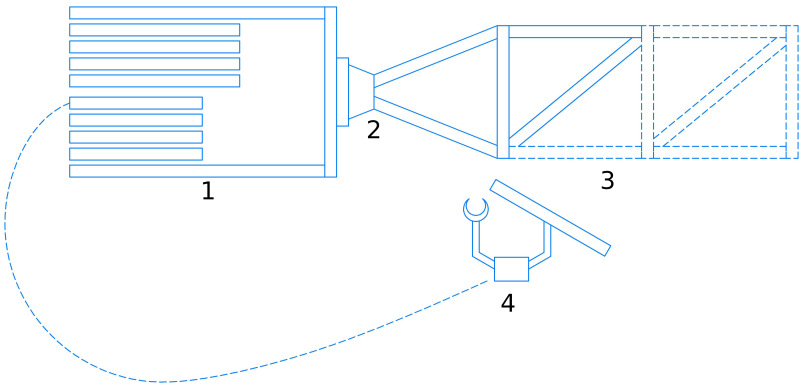

Figure 1. Considered objects: (**1**) cargo container, (**2**) installing platform, (**3**) truss structure, and (**4**) servicing spacecraft

It is assumed that the common center of mass of the considered objects are in a circular Earth orbit at the initial time. During the assembly process, TS rods must be transferred from their initial position in the CC to their target position (rod installation point) in a predetermined sequence and fixed on the TS. The CC, installation platform, and TS are all considered as a single unified rigid body (UB) during the SS's free motion. When the SS is fixed to the CC or TS, it is also a part of the UB.

During the free motion, the SS is considered as a point mass, even if the SS holds a rod. The attitude motion of the SS is not considered in this paper. It is assumed that, during the motion, the SS's center of mass remains outside the UB convex hull, as shown in Figure 2. Additionally, it is assumed that the attitude control system is capable of maintaining the rod perpendicular to the normal position of the UB convex hull, which prevents the collision of the rod with the UB, as shown in Figure 2.

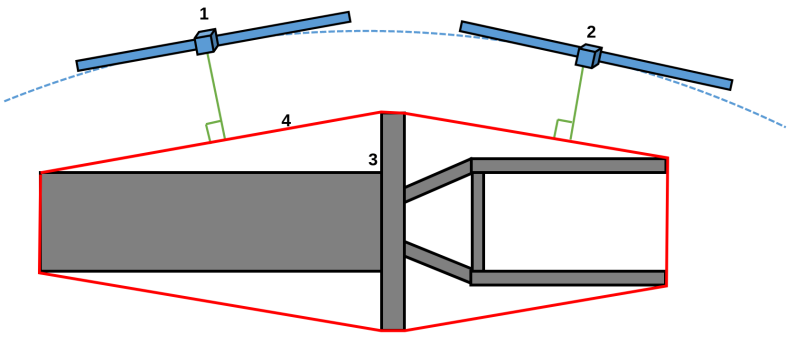

Figure 2. Angular motion of SS with rod: (**1**,**2**) two positions of servicing spacecraft with rod, (**3**) united body, and (**4**) united body convex hull

The considered objects' motion is described using the following reference frames:

- The structure reference frame (SRF) $A\tilde{x}\tilde{y}\tilde{z}$ is fixed to the CC, point A is the defined point of the CC, and the axes are a right-handed triad. The coordinates of the TS rods' edge points, of the CC's center of mass, and of the installing platform's position are defined in SRF and they are assumed to be constant. The SS's start point is defined by the radius-vector $\boldsymbol{r}_0^{SRF}$ in SRF; the SS's target point $\boldsymbol{r}_1^{SRF}$ for the SS's free motion remains constant in SRF during the flight.
- The body reference frame (BRF) $C\tilde{x}\tilde{y}\tilde{z}$ axes are aligned with the SRF axes, although BRF's origin point C is located at the UB center of mass.

- The inertial reference frame (IRF) C_EXYZ origin C_E is located in the Earth's center of mass, the Z-axis is directed along the Earth's rotation axis, the X-axis is directed towards the vernal equinox, and the Y-axis completes the right-handed triad.
- The orbital reference frame (ORF) $Oxyz$ has its origin O at the system common center of mass at an initial time, and point O moves along the circular orbit with radius R_{orb}. During the motion, the the system's common center of mass can deviate from point O. The z-axis of ORF is co-directed with the local vertical direction and the y-axis aligns with the orbital angular momentum; the x-axis completes the right-handed triad.

The transition between these reference frames is described by the following rotation matrices:

$$\begin{gathered}\boldsymbol{A}: IRF \rightarrow BRF,\\ \boldsymbol{U}: IRF \rightarrow ORF,\\ \boldsymbol{S}: ORF \rightarrow BRF.\end{gathered}$$

If the SS is located at a certain point $\boldsymbol{r}_0^{SRF}$ on the UB, it is assumed that the UB and SS move as a single rigid body. It is assumed that a set of initial state parameters, denoted by $\mathfrak{X}$, is known before the SS's repulsion time t_0^-. The parameter set $\mathfrak{X}$ is defined as follows:

$$\mathfrak{X} = [\boldsymbol{\omega}_{UB}^{IRF}(t_0^-), \boldsymbol{r}_{UB}^{ORF}(t_0^-), \boldsymbol{v}_{UB}^{ORF}(t_0^-), \boldsymbol{A}(t_0^-), \boldsymbol{U}(t_0^-)]^T,$$

where $\boldsymbol{\omega}_{UB}^{IRF}$ is the UB's angular velocity vector expressed in IRF, $\boldsymbol{r}_{UB}^{ORF}$ is the UB's center of mass's radius-vector in ORF, and $\boldsymbol{v}_{UB}^{ORF}$ is the UB's center of mass's velocity vector in ORF. These defined initial conditions and repulsion velocity vector $\boldsymbol{v}_0^{SRF}$ expressed in SRF determine the further angular and transnational motion of the UB and free motion trajectory of the SS's center of mass. Hence, $\mathfrak{X}$ and $\boldsymbol{v}_0^{SRF}$ define the final SS trajectory end point $\boldsymbol{r}_f^{SRF}$ at given time t_f. The mathematical problem considered in this paper is to find such a repulsion velocity vector $\boldsymbol{v}_0^{SRF}$ that leads the SS's trajectory end point $\boldsymbol{r}_f^{SRF}$ to the target point $\boldsymbol{r}_1^{SRF}$ with a defined acceptable error ε:

$$\boldsymbol{v}_0^{SRF}: \quad \Delta r = |\boldsymbol{r}_f^{SRF} - \boldsymbol{r}_1^{SRF}| < \varepsilon, \tag{1}$$

where ε can be defined as the length of the SS's manipulator capable of catching the final TS point.

This problem statement is formulated for a single SS transfer between two UB points. On-orbit TS assembly can be implemented by a sequence of such SS transfers between the CC's initial point and rods' installation points. For each transfer problem to be solved, the UB's initial conditions are different; during the assembly, the UB's mass distribution is changing, and additional constraints on the SS's relative trajectories are to be addressed in order to avoid collision.

3. Equations of Motion

In this paper, the translational motion of the UB's center of mass and the SS's center of mass are considered in the ORF. The attitude motion of the UB is also considered relative to ORF. The problem of the SS's attitude motion can be separated from the translational motion and it is out of scope of this paper.

The motion of the UB or the SS's center mass's position vector $\boldsymbol{r}^{ORF} = [x, y, z]^T$ is described by the Clohessy–Wiltshire Equations [26]:

$$\ddot{\boldsymbol{r}}^{ORF} = \begin{bmatrix}\ddot{x}\\ \ddot{y}\\ \ddot{z}\end{bmatrix} = \begin{bmatrix}-2\omega_0\dot{z}\\ -\omega_0^2 y\\ 3\omega_0^2 z + 2\omega_0\dot{x}\end{bmatrix}, \tag{2}$$

where $\omega_0 = \sqrt{\frac{\mu}{R_{\text{orb}}^3}}$ is the orbital angular velocity, μ is the Earth gravitational parameter, and R_{orb}^3 is the circular orbit radius. This system of differential equations has the following solution:

$$\boldsymbol{r}^{ORF} = \begin{bmatrix} C_4 - 3C_1\omega_0(t-t_0) + 2C_2\cos(\omega_0(t-t_0)) - 2C_3\sin(\omega_0(t-t_0)) \\ C_5\sin(\omega_0(t-t_0)) + C_6\cos(\omega_0(t-t_0)) \\ 2C_1 + C_2\sin(\omega_0(t-t_0)) + C_3\cos(\omega_0(t-t_0)) \end{bmatrix}, \quad (3)$$

where $C_1 - C_6$ are the trajectory parameters, which depend on the initial conditions defined by $\boldsymbol{r}^{ORF}(t_0)$ and $\dot{\boldsymbol{r}}^{ORF}(t_0)$ as follows:

$$\begin{array}{cc} C_1 = 2z(t_0) + \frac{\dot{x}(t_0)}{\omega_0}, & C_2 = \frac{\dot{z}(t_0)}{\omega_0}, \\ C_3 = -3z(t_0) - \frac{2\dot{x}(t_0)}{\omega_0}, & C_4 = x(t_0) - \frac{2\dot{z}(t_0)}{\omega_0}, \\ C_5 = \frac{\dot{y}(t_0)}{\omega_0}, & C_6 = y(t_0). \end{array}$$

These equations are valid for small distances relative to the ORF origin.

The attitude motion of the UB is described by Euler's dynamical equations and kinematic relations expressed in attitude quaternions:

$$J\dot{\boldsymbol{\omega}}^{BRF} + [\boldsymbol{\omega}^{BRF} \times \boldsymbol{J}\boldsymbol{\omega}^{BRF}] = \boldsymbol{m}_{ex}^{BRF}, \quad (4)$$

$$\dot{\Lambda} = \frac{1}{2}\Lambda \circ \boldsymbol{\omega}^{BRF}, \quad (5)$$

where $\boldsymbol{J}$ is the UB's inertia tensor calculated in BRF, $\boldsymbol{\omega}^{BRF}$ is the absolute angular velocity expressed in BRF, $\boldsymbol{m}_{ex}^{BRF}$ is the external torque, and Λ is the attitude quaternion. In this paper, external torque is a gravitational torque [27]:

$$\boldsymbol{m}_{ex} = \boldsymbol{m}_{grav} = 3\frac{\mu}{|r_{UB}|^5}\boldsymbol{r}_{UB} \times \boldsymbol{J}\boldsymbol{r}_{UB},$$

where $\boldsymbol{r}_{UB}$ is the radius-vector from Earth's center to the UB's center of mass written in BRF.

During the SS's free-flight motion and when the SS is fixed at the UB, the inertia tensor $\boldsymbol{J}$ remains constant in SRF and BRF, though at time moments when the SS repels and catches the UB, the $\boldsymbol{J}$ changes instantly due to the changed mass distribution. The tensor $\boldsymbol{J}$ can be calculated as sum of the UB modules' inertia tensors $\boldsymbol{J}^k$. Rods can be approximated as line segments with the following elements J_{ij}^k, of the inertia tensor:

$$J_{ij}^k = \int_{r_1}^{r_2}(\delta_{ij}r^2 - r_i r_j)dm = m_k\int_0^1(\delta_{ij}r^2 - r_i r_j)d\tau, \;\; \boldsymbol{r} = \boldsymbol{r}_1^k\tau + \boldsymbol{r}_2^k(1-\tau).$$

where $\boldsymbol{r}_1^k$ and $\boldsymbol{r}_2^k$ are the vectors of the kth rod ends in BRF, $i, j = 1, 2, 3$, m_k is the kth rod mass, and δ_{ij} is the Kronecker delta. Since the UB's center of mass changes its position during the assembly, the inertia tensor is calculated in SRF. According to the Huygens–Steiner theorem, the elements of $\boldsymbol{J}$ are translated into BRF as follows:

$$J_{ij}^{BRF} = J_{ij}^{SRF} - m_{UB}\left(|\boldsymbol{r}_{UB}^{SRF}|^2\delta_{ij} - r_{UB,\,i}^{SRF}r_{UB,\,j}^{SRF}\right),$$

where m_{UB} is the UB's mass, and $\boldsymbol{r}_{UB}^{SRF}$ is the vector between the centers of SRF and BRF.

4. Initial Conditions after the SS's Repulsion

The translational motion Equation (2) and attitude motion Equations (4) and (5) define the SS and the UB's trajectories if the initial conditions are specified. When the SS repulses from the UB or catches the TS target point, it sets new initial conditions for motion equations and it changes the UB's mass distribution. The SS repulsion's velocity vector

$\boldsymbol{v}_0^{SRF}$ is considered as an input parameter for achieving the required SS trajectory relative to the UB.

It is assumed that the SS's repulsion and capture using manipulators occurs instantly. The control of the manipulator motion during the repulsion to achieve the desired velocity $\boldsymbol{v}_0^{SRF}$ of the SS's center of mass relative to the UB is not considered in this paper. It is required to find such a repulsion velocity vector $\boldsymbol{v}_{SS}^{SRF+}$ in order to obtain the desired SS trajectory to get into the neighborhood of the target point $\boldsymbol{r}_1^{SRF}$, i.e., to solve the problem (1).

The initial conditions for motion in Equation (2) are to be specified in ORF, though the position of the SS at the time of repulsion and repulsion velocity are defined in SRF. Thus, first, the SS and the UB's centers of mass after repulsion should be expressed in ORF. Second, the SS's initial velocity after the repulsion is to be calculated in ORF taking into account the UB's angular velocity. Furthermore, the UB's initial velocity taking into account the influence of the SS's repulsion is to be corrected. Furthermore, finally, the UB's angular velocity after the repulsion as an initial condition for the attitude motion of Equation (4) should be defined.

In this section, subscripts $()^-$ and $()^+$ denote variables before and after the SS's repulsion, respectively. Let $\boldsymbol{r}_{UB}^{SRF-}$ be the radius-vector of the UB's center of mass C_{UB}^- with attached SS, and the radius-vector of the SS before the repulsion is denoted as $\boldsymbol{r}_{SS}^{SRF-}$. After the SS's repulsion, the UB's center of mass C_{UB}^+ radius-vector changes to $\boldsymbol{r}_{UB}^{SRF+}$. It is assumed that the SS's radius-vector immediately after the repulsion $\boldsymbol{r}_{UB}^{SRF+}$ is the same as before the repulsion, i.e., $\boldsymbol{r}_{UB}^{SRF-} = \boldsymbol{r}_{UB}^{SRF+}$. In this paper, the SS and UB's center of mass's trajectories are expressed in ORF. The radius-vectors of the UB and SS in ORF are defined by the following equations:

$$\boldsymbol{r}_{UB}^{ORF+} = \boldsymbol{r}_{UB}^{ORF-} + \boldsymbol{S}^T(\boldsymbol{r}_{UB}^{SRF+} - \boldsymbol{r}_{UB}^{SRF-}), \tag{6}$$

$$\boldsymbol{r}_{SS}^{ORF+} = \boldsymbol{r}_{UB}^{ORF-} + \boldsymbol{S}^T(\boldsymbol{r}_{SS}^{SRF+} - \boldsymbol{r}_{UB}^{SRF-}). \tag{7}$$

where $\boldsymbol{r}_{UB}^{ORF-}$ is the UB's center of mass defined in ORF before the repulsion. Here, the SS's position in SRF does not change instantly because of repulsion $\boldsymbol{r}_{SS}^{SRF-} = \boldsymbol{r}_{SS}^{SRF+}$, but the UB's center of mass is changed $\boldsymbol{r}_{UB}^{SRF-} \neq \boldsymbol{r}_{UB}^{SRF+}$ due to the SS's separation from the UB. The scheme of the system before and after the repulsion is presented in Figure 3.

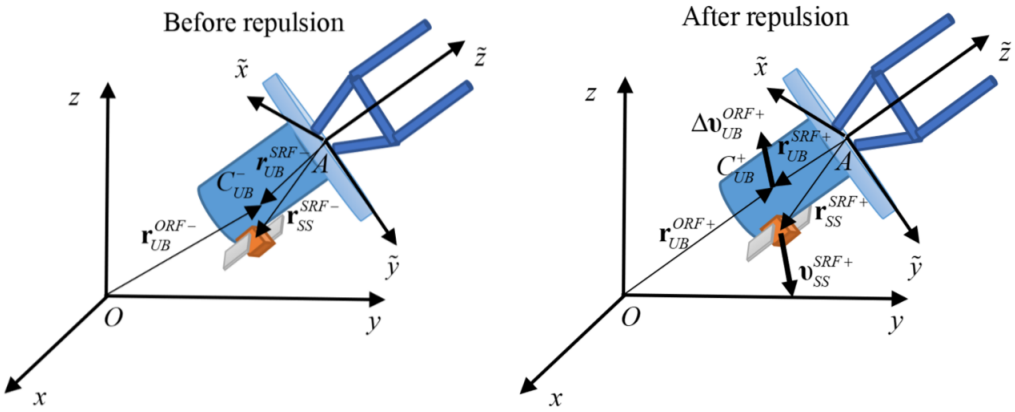

Figure 3. Scheme of system before and after servicing spacecraft's repulsion.

To calculate the instant change in velocities of the centers of mass due to the SS's repulsion, it is assumed that, during the short time of repulsion, the external forces do not change the momentum of the whole system, so the momentum conservation law is used. The momentum of the system expressed in ORF before the repulsion and after is as follows:

$$(m_{SS} + m_{UB})\boldsymbol{v}_{UB}^{ORF\,-} = m_{SS}\boldsymbol{v}_{SS}^{ORF\,+} + m_{UB}\boldsymbol{v}_{UB}^{ORF\,+}, \tag{8}$$

where m_{SS} is the mass of the SS and m_{UB} is the mass of UB without the SS, and $\boldsymbol{v}_{UB}^{ORF\,-}$ and $\boldsymbol{v}_{UB}^{ORF\,+}$ are the UB's center of mass's velocity vectors defined in ORF right before the repulsion and immediately after the repulsion, respectively. Since the ORF is a non-inertial reference frame, the effect of the non-inertial forces is also neglected due to the short time period of the repulsion. The velocities of the UB and SS's centers of mass in ORF is the sum of the instant velocity of the corresponding UB points before the repulsion and relative velocity due to the SS's repulsion. Since the UB is rotating with an angular velocity vector $\boldsymbol{\omega}_{UB}^{ORF\,-}$ before the repulsion, and the UB's center of mass changes its position, angular velocities $\boldsymbol{v}_{UB}^{ORF\,+}$ and $\boldsymbol{v}_{SS}^{ORF\,+}$ are defined as follows:

$$\boldsymbol{v}_{UB}^{ORF\,+} = \boldsymbol{v}_{UB}^{ORF\,-} + [\boldsymbol{\omega}_{UB}^{ORF\,-} \times (\boldsymbol{r}_{UB}^{ORF\,+} - \boldsymbol{r}_{UB}^{ORF\,-})] + \Delta\boldsymbol{v}_{UB}^{ORF\,+}, \tag{9}$$

$$\boldsymbol{v}_{SS}^{ORF\,+} = \boldsymbol{v}_{UB}^{ORF\,-} + [\boldsymbol{\omega}_{UB}^{ORF\,-} \times (\boldsymbol{r}_{SS}^{ORF\,+} - \boldsymbol{r}_{UB}^{ORF\,-})] + \Delta\boldsymbol{v}_{SS}^{ORF\,+}, \tag{10}$$

where $\Delta\boldsymbol{v}_{UB}^{ORF\,+}$ is the change in the UB's center of mass's velocity due to the SS's repulsion, and $\Delta\boldsymbol{v}_{SS}^{ORF\,+}$ is the vector of SS's repulsion velocity defined in ORF. Substituting (9) and (10) into (8) and taking into account the relation between the vectors of the UB's center of mass before $\boldsymbol{r}_{UB}^{ORF\,-}$ and after the repulsion $\boldsymbol{r}_{UB}^{ORF\,+}$,

$$\boldsymbol{r}_{UB}^{ORF\,-} = \frac{m_{SS}\boldsymbol{r}_{SS}^{ORF\,+} + m_{UB}\boldsymbol{r}_{UB}^{ORF\,+}}{m_{SS} + m_{UB}}, \tag{11}$$

the following relation between the change in the UB's center of mass's velocity $\Delta\boldsymbol{v}_{UB}^{ORF\,+}$ and the SS's repulsion velocity $\Delta\boldsymbol{v}_{SS}^{ORF\,+}$ can be obtained:

$$\Delta\boldsymbol{v}_{UB}^{ORF\,+} = -\frac{m_{SS}}{m_{UB}}\Delta\boldsymbol{v}_{SS}^{ORF\,+}. \tag{12}$$

The problem considered in the paper (1) is formulated to obtain the SS's repulsion velocity $\boldsymbol{v}_{SS}^{SRF\,+}$ in SRF; it can be obtained by the transition of $\Delta\boldsymbol{v}_{SS}^{ORF\,+}$ into SFR using a transition matrix $\boldsymbol{S}$ as follows:

$$\boldsymbol{v}_{SS}^{SRF\,+} = \boldsymbol{S}\Delta\boldsymbol{v}_{SS}^{ORF\,+}.$$

The SS's repulsion also results in the UB's angular velocity change. To calculate the UB's angular velocity after the repulsion $\boldsymbol{\omega}_{UB}^{ORF\,+}$, it is assumed that the external torques and torques due to non-inertial forces in ORF have no influence on the total angular momentum change of the system during the short repulsion time, so the angular momentum conservation law can be applied. Angular momentum in ORF is the sum of the UB's angular momentum and the momentum of the center of mass's impulses relative to the ORF. The following relation using the angular momentum conservation law written in ORF is obtained:

$$\begin{aligned} \boldsymbol{S}^T\boldsymbol{J}^-\boldsymbol{S}\boldsymbol{\omega}_{UB}^{ORF\,-} + [\boldsymbol{r}_{UB}^{ORF\,-} \times (m_{SS} + m_{UB})\boldsymbol{v}_{UB}^{ORF\,-}] = \\ = \boldsymbol{S}^T\boldsymbol{J}^+\boldsymbol{S}\boldsymbol{\omega}_{UB}^{ORF\,+} + [\boldsymbol{r}_{SS}^{ORF\,+} \times m_{SS}\boldsymbol{v}_{SS}^{ORF\,+}] + [\boldsymbol{r}_{UB}^{ORF\,+} \times m_{UB}\boldsymbol{v}_{UB}^{ORF\,+}], \end{aligned} \tag{13}$$

where $\boldsymbol{J}^-$ is the UB's (with attached SS) inertia tensor before the repulsion, and $\boldsymbol{J}^+$ is the UB's (without SS) inertia tensor after the repulsion. Since, in (13), all the values are written in ORF, the inertia tensor originally calculated in BRF is translated to ORF by $\boldsymbol{S}^T\boldsymbol{J}\boldsymbol{S}$. Thus, the angular velocity after the repulsion $\boldsymbol{\omega}_{UB}^{ORF\,+}$ can be obtained from (13) as follows:

$$\boldsymbol{\omega}_{UB}^{ORF\,+} = (\boldsymbol{S}^T\boldsymbol{J}^+\boldsymbol{S})^{-1}\begin{pmatrix} \boldsymbol{S}^T\boldsymbol{J}^-\boldsymbol{S}\boldsymbol{\omega}_{UB}^{ORF\,-} + [\boldsymbol{r}_{UB}^{ORF\,-} \times (m_{SS} + m_{UB})\boldsymbol{v}_{UB}^{ORF\,-}] - \\ -[\boldsymbol{r}_{SS}^{ORF\,+} \times m_{SS}\boldsymbol{v}_{SS}^{ORF\,+}] - [\boldsymbol{r}_{UB}^{ORF\,+} \times m_{UB}\boldsymbol{v}_{UB}^{ORF\,+}] \end{pmatrix}. \tag{14}$$

Thus, the UB and SS's center of mass's positions (6) and (7), the UB and SS's velocities (9) and (10), and the UB's angular velocity (14) all depend on the SS's repulsion velocity $\boldsymbol{v}_{SS}^{SRF+}$. These initial conditions after the repulsion define the SS's trajectory relative to the UB in SRF. So, the problem (1) of finding the SS's repulsion vector $\boldsymbol{v}_{SS}^{SRF+}$ to achieve the TS target point $\boldsymbol{r}_1^{SRF}$ can be formulated as boundary problem.

The change in the motion state parameters after the SS captures the TS target point is calculated using the same momentum and angular momentum conservation laws. The expressions for the UB's center of mass's position, velocity, and angular velocity are not provided in the paper for brevity. The initial conditions after the capture depend on the SS's relative velocity before the capture; it defines the UB's attitude and translational motion. Thus, UB's motion parameters are also can be controlled by the choice of the SS's repulsion velocity $\boldsymbol{v}_{SS}^{SRF+}$ in the sequential order of the SS's repulsion and capturing during the assembly process.

5. Planar Motion Case

First, we consider an approach to solve the problem (1) in a simplified motion case for a demonstration of the proposed on-orbit assembly scheme. Furthermore, the results of this section are later used as the initial guess for the numerical search algorithms in the spatial motion case.

The Clohessy–Wiltshire Equation (2) allows the separation the out-of-plane motion along the y-axis from the motion in the orbital plane Oxz. In this section, several assumptions are made about the system's motion:

- The position vectors of the SS's center of mass $\boldsymbol{r}_{SS}^{SRF}$ and the UB's center of mass $\boldsymbol{r}_{UB}^{SRF}$ have zero values for their y-axis components;
- The angular velocity $\boldsymbol{\omega}_{UB}^{ORF}$ of the UB has zero values for its x- and z-axis components;
- Gravitational torque is not considered;
- The inertia tensor $\boldsymbol{J}$ is reduced to a single y-axis moment of inertia I_y;
- The time duration of the SS's free flight after the repulsion $t_f - t_0$ is fixed.

So, such a system's motion is a plane-parallel motion in orbital plane Oxz. The considered planar motion is not a common motion case, it is just a particular example, allowing to simplify the calculations of the repulsion velocity's first guess for the spatial motion.

In this case, the final deviation of the trajectory point $\boldsymbol{r}_f^{SRF} = [x_f, 0, z_f]^T$ at time t_f from the target point $\boldsymbol{r}_1^{SRF} = [x_1, 0, z_1]^T$ in the TS only has two components Δx and Δz:

$$\Delta \boldsymbol{r}^{SRF} = [\Delta x, 0, \Delta z]^T = \boldsymbol{r}_1^{SRF} - \boldsymbol{r}_f^{SRF}.$$

As the result of the integration of motion Equations (2), (4) and (5), the deviation components Δx and Δz depend on a set of initial conditions $\mathfrak{X}$, the mass of the SS m_{SS}, the mass of the UB m_{UB}, and the moment of inertia I_y. This dependence is derived by analytically taking into account the change in the UB's translational velocity (12) and change in the UB's angular velocity (14). In the planar motion case, the SS's repulsion velocity vector $\boldsymbol{v}_{SS}^{SRF+} = [v_0^x, 0, v_0^z]^T$ also has only two nonzero components. The dependence of Δx and Δz on v_0^x and v_0^z has the following form:

$$\Delta x = x_1 + A_1 \cos B - A_2 \sin B, \qquad \Delta z = z_1 + A_1 \sin B + A_2 \cos B, \tag{15}$$

where

$$A_1 = a_1 v_0^x + a_2 v_0^z + a_3, \;\; A_2 = a_4 v_0^x + a_5 v_0^z + a_6, \;\; B = b_1 v_0^x + b_2 v_0^z + b_3.$$

Here, a set of coefficients a_i and b_i are calculated using the parameter set $\mathfrak{X}$ and mass-inertial parameters m_{SS}, m_{UB}, and I_y. Analytical expressions of a_i and b_i are omitted from the text since they are too bulky. The value of the parameter B is a final increment of the

UB's angle after the SS's free relative motion between the given time of repulsion t_0 and time of the SS attaching to the UB t_f:

$$B = \int_{t_0}^{t_f} \omega_y dt,$$

where ω_y is an angular velocity of the UB after the SS's repulsion, which is assumed to be constant since no external torques are taken into account in this section.

For the simplified case of motion considered, the problem (1) can be reformulated to find the exact solution that implies a zero-valued final trajectory deviation:

$$\{v_0^x, v_0^z\} : \Delta x = 0, \Delta z = 0. \tag{16}$$

Even for this simplified case, the problem (16) cannot be solved in explicit form because Equation (15) is nonlinear with respect to the repulsion velocity components v_0^x and v_0^z. So, the solution of problem (16) is to be found numerically. However, using additional assumptions, the approximate solutions can be found analytically.

For example, if it is assumed that the UB's rotation angle is small during the SS's free motion, the value of parameter B can be considered as zero in (15). Equation (15) is simplified to the following equation:

$$\Delta x \approx A_1 + x_1, \quad \Delta z \approx A_2 + z_1.$$

In this case, the approximate solution of the (16) is as follows:

$$v_0^x \approx \frac{a_2(a_6 + z_1) - a_5(a_3 + x_1)}{a_1 a_5 - a_2 a_4}, \qquad v_0^z \approx \frac{a_4(a_3 + x_1) - a_1(a_6 + z_1)}{a_1 a_5 - a_2 a_4}. \tag{17}$$

If coefficients a_i are significantly larger than coordinates x_1 and z_1, the approximate solution can be found from $A_1 = 0$ and $A_2 = 0$ and it can be further simplified:

$$v_0^x \approx \frac{a_2 a_6 - a_3 a_5}{a_1 a_5 - a_2 a_4}, \qquad v_0^z \approx \frac{a_3 a_4 - a_1 a_6}{a_1 a_5 - a_2 a_4}. \tag{18}$$

A particular example of a parameter set $\mathfrak{X}$ of initial conditions is demonstrated in Figure 4. The value of the separation velocity components v_0^x and v_0^z is limited by the 5 cm/s in this example. This limitation of velocity components is based on the next simple evaluation. If it is supposed that the manipulator produces a force of $F = 0.1$ N along an acceleration trace of $L = 50$ cm, and pushes the SS loaded with a rod with a total weight of $m = 35$ kg, then the velocity of the repulsion can be calculated according to the following expression obtained under the assumption of constant acceleration:

$$v = \sqrt{\frac{2LF}{m}} \approx 5.3 \text{ cm/s}.$$

The maximum length of the manipulator is defined as 1 m, so it is assumed that the acceptable final trajectory deviation must be less than this value. Using the dependence (15) of the trajectory deviation, components Δx and Δz on the separation velocity from the value of the final position deviation $\Delta r = |\Delta \boldsymbol{r}|$ can be calculated on a grid of v_0^x , $v_0^z \in [-5; 5]$ cm/s for the specified parameters. Figure 4 shows a heatmap of Δr and points of numerically obtained grid solution (with a resolution of 0.01 cm/s) and approximate solutions calculated using (17) and (18). For this particular case, the error of the repulsion velocity guesses are about 1 cm/s for (17) and about 1.5 cm/s for (18).

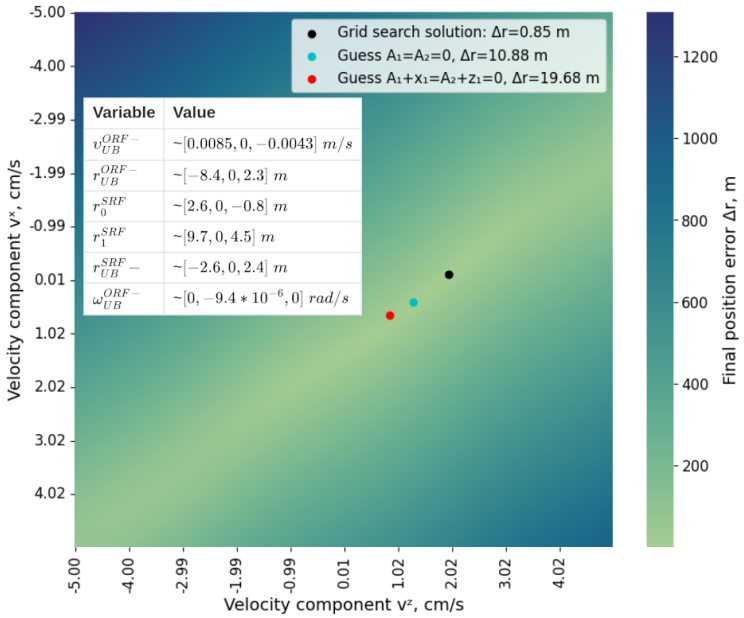

Figure 4. Example of distribution of final position deviation value Δr.

For a numerical study of the accuracy of approximate solutions (17) and (18), the random initial conditions and random initial and final points are considered; its standard deviation values are presented in the right side of Table 1. The resulting values of parameters a_i, b_i, x_1, and z_1 for random initial conditions are presented in Figure 5. Particularly, it can be seen that the assumption used for solution (18) that the coefficients a_i are significantly larger than coordinates x_1 and z_1 is correct. For each parameter values, the final deviation value Δr is calculated. The results of the calculations are presented as boxplots in Figure 6. Here, the boxplot (a) shows the error of final position calculation and the boxplot (b) provides the deviation of the repulsion velocity calculated by the approximate solution from the grid search solution. Inside the box, there are 50% of the simulations results, below and under the box are 25%, and the red line is a mean value. The obtained accuracy of several meters is unacceptable to use it for the SS's repulsion velocity calculation. However, this accuracy is considered acceptable as the initial guess for the numerical search of the solution (1) for the spatial motion case. As it can be concluded from Figure 4, the maximum value of the final position error can be up to 1200 m, and guess solutions (18) and (17) reduce this error by 10^2 times.

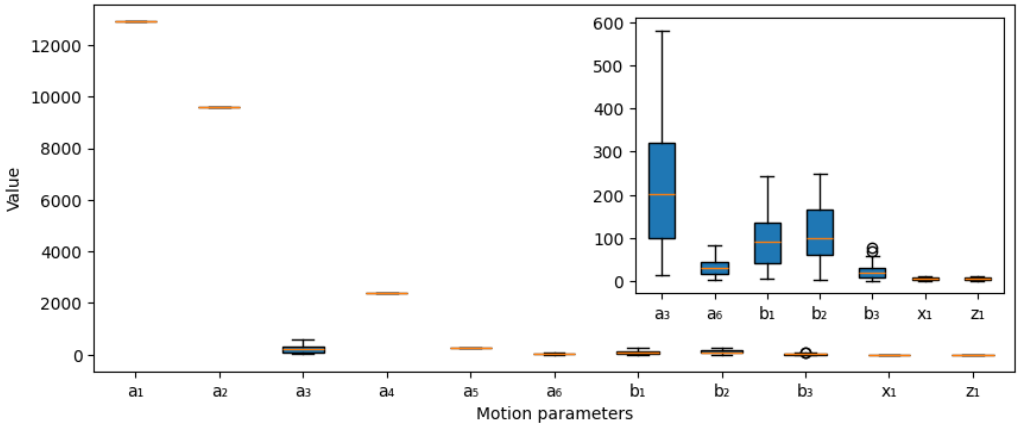

Figure 5. Values of motion parameters a_i, b_i, x_1, and z_1.

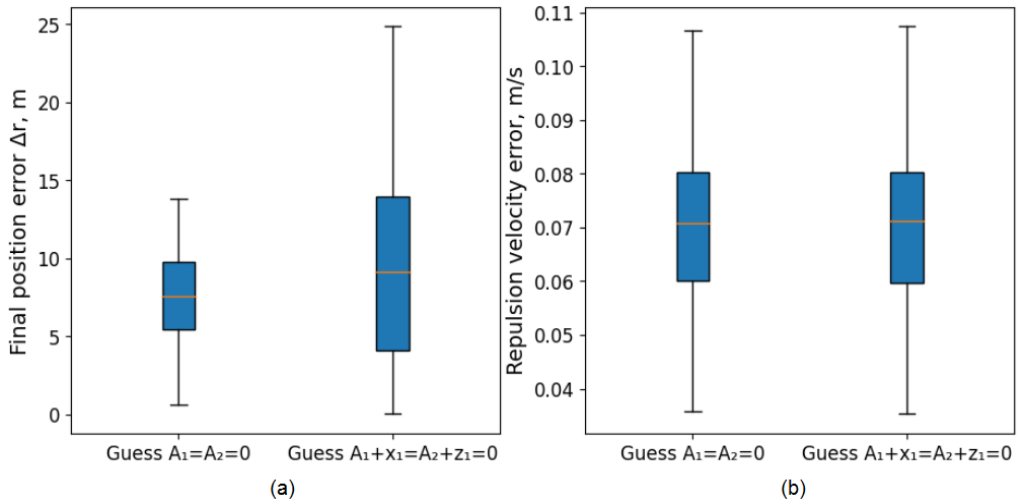

Figure 6. Boxplots of variation of the final position deviation (**a**) and of repulsion velocity error (**b**) ($N_{samples} = 100$).

Table 1. Numerical simulation parameters.

Parameter	Value	Value of Vectors	Standard Deviation
m_{SS}	20 kg	v_{UB}^{ORF-}	10^{-2} m/s
m_{UB}	650 kg	r_{UB}^{ORF-}	10 m
I_y^-	5600 kg·m^2	r_0^{SRF},r_1^{SRF}	10 m
$t_f - t_0$	4000 s	r_{UB}^{SRF}	5 m
R_{orb}	7000 km	ω_{UB}^{ORF-}	10^{-4} rad/s

In the case where the SS's repulsion velocity is limited by some feasible value, which can be implemented by the SS's manipulator, no solution could be found to the problem (1). It can be demonstrated in the planar motion case. Distributions of the final position deviation Δr in the repulsion velocity domain $\{v_0^x, v_0^z\} \in [-5; 5]$ cm/s for three values of UB's initial angular velocities are presented in Figure 7. The left two cases in Figure 7 with UB's initial angular velocities of 10^{-4} rad/s and 10^{-3} rad/s are solutions of the problem (16), while the right figure presents the case with an initial angular velocity of 7×10^{-3} rad/s, where the minimum of Δr corresponds to deviation of 40 m, which is unacceptable and the problem has no solution in this case.

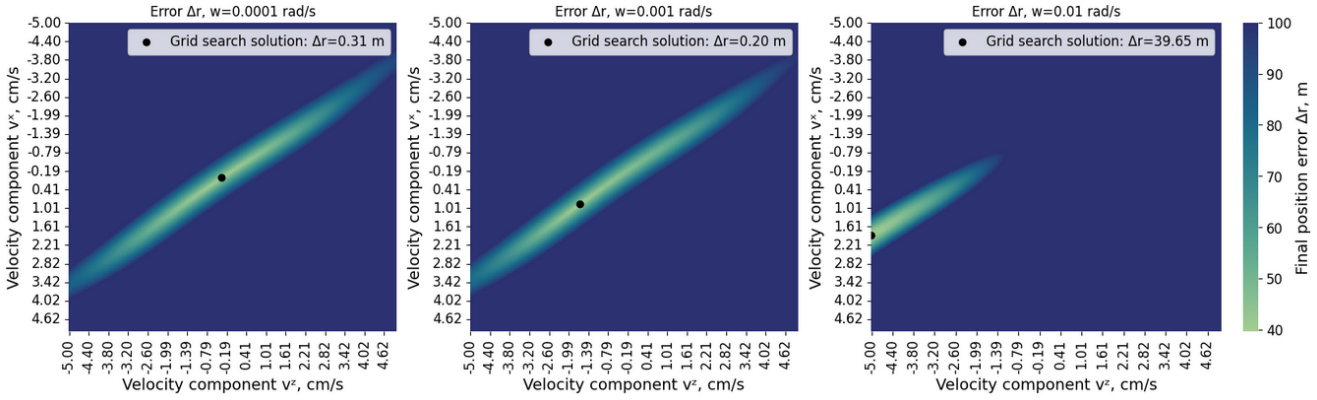

Figure 7. Solution existence depending on the united body's angular velocity ω.

6. Assembly in Spatial Motion Case

In a common spatial motion case, it is impossible to obtain the final trajectory deviation $\Delta \boldsymbol{r}$ in an analytical form as for the planar motion case (15), because the dynamical Euler Equation (4) has no analytical solution except for the three known attitude motion cases—the Euler, Lagrange, and Kovalevskaya cases. Since, in this study, the gravity-gradient torque is taken into account in the UB's attitude motion equation, and the inertia tensor is arbitrary and it changes during the assembly, it does not meet requirements of any of these three special attitude motion cases. Thus, the $\Delta \boldsymbol{r}$ dependence on the SS's repulsion velocity $\boldsymbol{v}_{SS}^{SRF\,+}$ can be obtained only by the numerical integration of the attitude and translational motion equations.

6.1. Constrained-Motion Parameters

In common motion case, the following set of additional requirements and constraints for the problem (1) is considered for taking into account the practical aspects of TS assembly:

- The SS's trajectory must not intersect the UB's elements to avoid collision with them except for the target point $\boldsymbol{r}_1^{SRF}$.
- Since, at a high UB angular velocity, the problem (1) could have no solution in the limited domain of the repulsion velocity values as it has been demonstrated in the planar motion case, the value of the UB's angular velocity $\boldsymbol{\omega}_{UB}^{ORF}$ after the TS's capture should not exceed an acceptable value.
- To maintain the UB's attitude in ORF in the vicinity of its initial attitude during the assembly, it can be additionally demanded that the UB's attitude deviation after the TS's capture should be inside the limited domain. It is reasonable to place initially the UB in the vicinity of the stable gravitational equilibrium attitude position and stay in this vicinity during the assembly.
- During the assembly, the UB's center of mass can significantly deviate from the origin of the ORF moving along the circular orbit. In order to prevent possibly undesirable deviation from the initial orbit, the UB's center of mass's position $\boldsymbol{r}_{UB}^{ORF}$ and velocity $\boldsymbol{v}_{UB}^{ORF}$ must be kept within prescribed limits.

In order to address these limitations during the assembly, in this work, the following vector $\boldsymbol{c}$ of the UB's motion-constrained parameters is taken into account in the numerical search of the problem (1)'s solution:

$$\boldsymbol{c} = \left[|\boldsymbol{r}_{UB}^{ORF}|, |\boldsymbol{v}_{UB}^{ORF}|, |\boldsymbol{\omega}_{UB}^{ORF}| \right]^T. \tag{19}$$

To meet the requirements of the SS's relative trajectory to prevent the collision with the TS, the following approaches are proposed:

- Approach 1. During the numerical search of the repulsion velocity, the final position deviation $\Delta \boldsymbol{r}$ is calculated using the integration of the attitude and translational motion equations. At each integration point of the SS's center of mass's position, the minimum distance with the UB's points approximated by a grid is calculated. If this distance is less than the defined characteristic size of the SS, it is assumed that the trajectory intersects the UB. At this point $\boldsymbol{r}_c^{SRF}$, the integration of the motion equations stops and the deviation is calculated as $\Delta \boldsymbol{r} = \boldsymbol{r}_c^{SRF} - \boldsymbol{r}_1^{SRF}$. If $|\Delta \boldsymbol{r}| > \varepsilon$; then, it is assumed that the trajectory collides with UB's elements and the numerical search continues. If $|\Delta \boldsymbol{r}| < \varepsilon$, then it is assumed that solution of the problem (1) is found.
- Approach 2. Another approach is to consider a continuous function g to describe the trajectory intersection with the UB's elements. Function g is used to define the hyper-quadratic potential field in the vicinity of the structure; this approach for structure assembly was proposed in [28]. Function g is positive if the SS is outside the UB's elements, and negative if the SS is inside. Since the UB consists of a container and a set of rods, which can be considered as elongated bodies, the following function g is used to describe the potential field for a cylinder:

$$g = \begin{cases} \frac{d}{2}(\sqrt{\rho_y^2 + \rho_z^2} - 1), & -1 < \rho_x < 1, \\ \frac{l}{2}(|\rho_x| - 1), & else\ if\ \rho_y^2 + \rho_z^2 < 1, \\ \frac{d}{2}(\sqrt{\rho_y^2 + \rho_z^2} - 1) + \frac{l}{2}(|\rho_x| - 1), & else, \end{cases} \quad (20)$$

where d is a rod diameter, l is the rod length, and ρ_x, ρ_y, and ρ_z, are dimensionless projections of the position vector $\boldsymbol{r}_{SS}$ onto the rod-fixed reference frame. A schematic heatmap of the g function for a cylinder is shown in Figure 8. In this example, the length of the cylinder is 2 m and its diameter is 1 m; the boundaries of the rod are represented by blue lines in Figure 8. With defined UB element positions in SRF, a sum of the functions g_i corresponding to each element forms a final potential field of the UB. If the SS's trajectory does not intersect the UB, each function g_i must remain strictly positive or be higher than some positive value to prevent the collision. These functions can also be included in the vector of constrained parameters $\boldsymbol{c}$ in (19) for a numerical search of the SS's repulsion velocity.

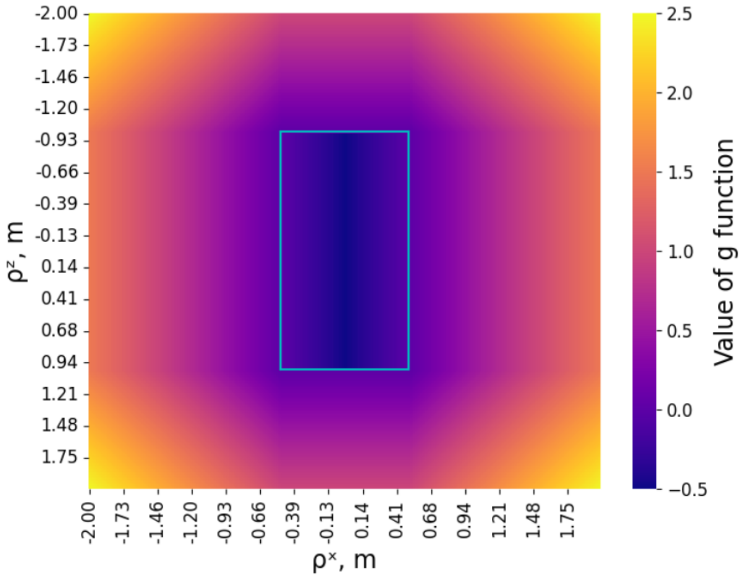

Figure 8. Heatmap of function g; the boundaries of the rod are represented by blue lines.

6.2. Target Function for the Numerical Search

For a numerical search of the SS's repulsion velocity $\boldsymbol{v}_0 = \boldsymbol{v}_{SS}^{SRF+}$ taking into account constrained-motion parameters, the original problem (1) is reformulated using the following target function $\Phi(\boldsymbol{v}_0)$:

$$\begin{cases} \boldsymbol{v}_0: \quad \Phi(\boldsymbol{v}_0) = \Delta \boldsymbol{r}^2 \to min, \\ c_i^{max} - c_i \geqslant 0, \quad i = 1 \ldots N, \end{cases} \quad (21)$$

where $\boldsymbol{v}_0 \in D$, $D \in R^3$ is a feasible region of velocity vector $\boldsymbol{v}_0$, $\Delta \boldsymbol{r}$ is final trajectory deviation vector $\Delta \boldsymbol{r} = \boldsymbol{r}_1^{SRF} - \boldsymbol{r}_f^{SRF}$, $\boldsymbol{c} = [c_1, \ldots c_N]^T$ is vector of constrained variables, and $\boldsymbol{c}^{max} = [c_1^{max}, \ldots c_N^{max}]^T$ is the vector of maximal acceptable values of the constrained parameters. The problem (21) can then be transformed into an unconditional problem using the barrier or penalty function introduced in [29]:

$$\Phi_{barrier}(\boldsymbol{v}_0, \boldsymbol{c}) = \Phi(\boldsymbol{v}_0) - \mu \sum_{i=1}^{N} log\left(1 - \frac{c_i}{c_i^{max}}\right),$$

$$\Phi_{penalty}(\boldsymbol{v}_0, \boldsymbol{c}) = \Phi(\boldsymbol{v}_0) - \mu \sum_{i=1}^{N} \left(1 - \frac{c_i}{c_i^{max}}\right)_+,$$

where $\mu > 0$ is a small positive parameter and $(\ )_+$ represents the rectified linear unit (ReLU) function. However, the $\Phi_{barrier}$ function is undefined if the constraints are not fulfilled, which may cause the non-convergence during the minimization of the function. The $\Phi_{penalty}$ function highly depends on parameter μ and it only counts constraints in the constraint-violation area. These features may lead to a local minimum of the function that is not the solution of the problem (1). Thus, a new function is required that is characterized by the given functions' advantages, but does not have their shortcomings. That is why, in this paper, the following barrier function is proposed:

$$\begin{cases} \Phi^*(\boldsymbol{v}_0, \boldsymbol{c}) = \Phi(\boldsymbol{v}_0) - \mu \sum_{i=1}^{m} log(\varepsilon_i), \\ \varepsilon_i = \begin{cases} 1 - \frac{c_i}{c_i^{max}} + \delta \frac{c_i}{c_i^{max}}, & (1 - \frac{c_i}{c_i^{max}}) \geqslant 0, \\ \delta e^{1 - \frac{c_i}{c_i^{max}}}, & (1 - \frac{c_i}{c_i^{max}}) < 0, \end{cases} \end{cases} \tag{22}$$

where δ is the hyperparameter that connects the function $\Phi^*(\boldsymbol{v}_0)$ defined in the constraint-fulfilled domain with the function $\Phi^*(\boldsymbol{v}_0)$ defined in the constraint-violated domain. In the case where $\delta \ll 1$, the function $\Phi^*(\boldsymbol{v}_0)$ represents a penalty function in the constraint-violated domain. An example of the logarithm argument function $\varepsilon(\frac{c_i}{c_i^{max}})$ and the function $\Phi^*(\frac{c_i}{c_i^{max}})$ dependence on the ratio $\frac{c_i}{c_i^{max}}$ using different values of δ is shown in Figure 9. From the figure, it can be concluded that the function $\Phi^*(\frac{c_i}{c_i^{max}})$ is smooth and the gradient minimization methods can be applied for the numerical solution search.

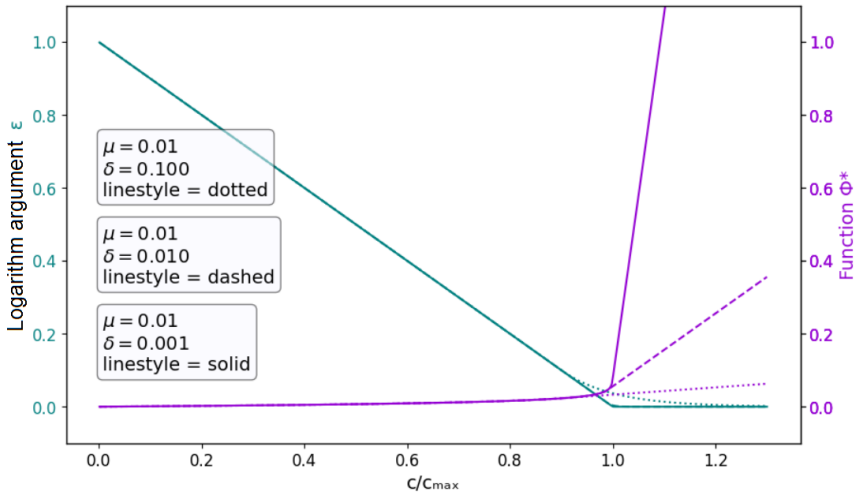

Figure 9. Example of dependence $\varepsilon(\frac{c_i}{c_i^{max}})$ and $\Phi^*(\frac{c_i}{c_i^{max}})$ on ratio $\frac{c_i}{c_i^{max}}$ for several δ values.

6.3. Repulsion Velocity's Initial Guess

The performance of many numerical minimization methods strongly depends on the initial guess. Gradient-based methods are prone to converge to a local minimum when searching the parameter area where the initial guess vector is defined. So, this aspect of numerical search is of high importance in this work. This paper proposes two approaches to calculate an initial guess for the SS's repulsion velocity $\boldsymbol{v}_0^*$ using the following simplified motion cases:

(1) The planar motion case described in Section 5 is used for the initial guess $\boldsymbol{v}_0^* = [v_0^x, 0, v_0^z]^T$'s calculation according to (18).

(2) In the spatial motion case, under the assumption that the UB's position and attitude are fixed in ORF, the following initial guess $\boldsymbol{v}_0^* = [v_0^x, v_0^y, v_0^z]^T$ using the solution (3) of the Clohessy–Wiltshire Equation (2) is calculated according to [25]:

$$\begin{aligned} v_0^x &= \frac{\omega_0\left((6\Delta t\omega_0 z_0 + x_1 - x_0)\sin(\Delta t\omega_0) + (14z_0 - 2z_1)(\cos(\Delta t\omega_0) - 1)\right)}{-3\Delta t\omega_0 \sin(\omega_0\Delta t) - 8\cos(\omega_0\Delta t) + 8}, \\ v_0^y &= \frac{\omega_0(-y_0\cos(\omega_0\Delta t) + y_1)}{\sin(\omega_0\Delta t)}, \\ v_0^z &= \frac{\omega_0\left((3\Delta t\omega_0 z_0 + 2x_1 - 2x_0)\cos(\Delta t\omega_0) - 3\Delta t\omega_0 z_1 + 2x_0 - 2x_1 + 4(z_1 - z_0)\sin(\Delta t\omega_0)\right)}{-3\Delta t\omega_0 \sin(\omega_0\Delta t) - 8\cos(\omega_0\Delta t) + 8}, \end{aligned} \tag{23}$$

where $\boldsymbol{r}_0^{ORF} = [x_0, y_0, z_0]^T$ is the SS's start point, $\boldsymbol{r}_1^{ORF} = [x_1, y_1, z_1]^T$ is the SS's target point, and $\Delta t = t - t_0$ is defined time of the SS's free flight. It can be concluded from (23) that the selection of the flight time Δt strongly affects the SS's repulsion velocity and, as a sequence, it affects the SS's trajectory. Furthermore, it follows from (23) that the flight time multiplication to half of the orbital period $\Delta t = \pi k/\omega_0, k = 1, 2, 3, \ldots, n$ is unacceptable; it leads to infinite repulsion velocity and it means that there is no solution to the boundary problem. In this paper, for an acceptable initial guess search, a set of SS's flight times is considered $\Delta \boldsymbol{t} = [\Delta t^1, \ldots, \Delta t^k]^T$; for each Δt^i, the repulsion velocity $\mathbf{Y} = [\boldsymbol{v}_0^1, \ldots \boldsymbol{v}_0^k]$ is calculated using (23) and the trajectory collision avoidance requirement is roughly checked. It is assumed that the forbidden zone for the trajectory is a sphere with a diameter with endpoints $\boldsymbol{r}_0^{ORF}$ and $\boldsymbol{r}_1^{ORF}$. The SS's trajectory with repulsion velocity $\boldsymbol{v}_0^i$ can be roughly considered as a set of SS's positions $\boldsymbol{r}_j^i$ with m points. The repulsion velocity $\boldsymbol{v}_0^i$ is specified as being invalid if the following inequality is true:

$$\exists j: \quad \left|\boldsymbol{r}_j^i - \frac{1}{2}(\boldsymbol{r}_0^{ORF} + \boldsymbol{r}_1^{ORF})\right| < \frac{1}{2}\left|\boldsymbol{r}_0^{ORF} - \boldsymbol{r}_1^{ORF}\right|, j = 1, \ldots, m. \tag{24}$$

This condition corresponds to the case when the SS's radius-vector from the sphere center is less than the sphere radius. Using (24), the repulsion velocity for the acceptable initial guess in terms of preliminary rough collision avoidance requirements and corresponding flight time Δt is selected.

6.4. Numerical Search Algorithms

Two numerical search algorithms were used in this paper to solve problem (21) depending on the proposed above approaches to address the SS's collision avoidance aspect:

- Algorithm 1. For the case of using Approach 1 from Section 6.1, when the numerical integration stops when the SS's trajectory intersects the UB's element during the search for the solution, and when the vector of constrained parameters $\boldsymbol{c}$ from (19) is short (it does not include the g functions), then Newton's method was used in this paper to solve the problem (21). Newton's method iteratively calculates the repulsion velocity using the following formula [30]:

$$\boldsymbol{v_0}^{i+1} = \boldsymbol{v_0}^i - \left(\frac{\partial \nabla\Phi}{\partial \boldsymbol{v_0}}\Big|_{\boldsymbol{v_0}=\boldsymbol{v_0}^i}\right)^{-1} \nabla\Phi\Big|_{\boldsymbol{v_0}=\boldsymbol{v_0}^i}, \tag{25}$$

where i is the iteration number of the method, and $\nabla\Phi$ is the gradient vector of the target function (22):

$$\nabla\Phi = \left[\frac{\partial\Phi}{\partial v_0^x}, \frac{\partial\Phi}{\partial v_0^y}, \frac{\partial\Phi}{\partial v_0^z}\right]^T.$$

The iterative procedure stops if the norm of the difference of two sequential values of $\boldsymbol{v_0}^{i+1}$ is less than the defined small value ε_{v_0}: $\left|\boldsymbol{v_0}^{i+1} - \boldsymbol{v_0}^i\right| < \varepsilon_{v_0}$.

- Algorithm 2. For the case of using the Approach 2 from Section 6.1, when the functions g (20) are added to the vector of constrained parameters $\boldsymbol{c}$ to address the collision avoidance, the trust region [30] method from the Python library "scipy" was used. This method is based on a subset of the objective function region that is approximated using a model quadratic function. If an appropriate approximation of the objective function is found within the trust region, then the searching region is expanded; conversely, if the approximation is poor, then the region is contracted. The criterion for appropriate approximation is the improvement of the objective function value.

Both algorithms were used for the numerical search for the problem's solution. Algorithm 1 is faster than Algorithm 2, though Algorithm 1 is more sensitive to the initial velocity guess. The main reason that Algorithm 2 runs significantly slower is that the solution for the problem $\Phi(\boldsymbol{v}_0) \rightarrow min$ (21) is searched on the boundary of fulfilling constraints $c_i^{max} - c_i \geqslant 0$. So, the more computationally complex Algorithm 2 is used for the repulsion velocity search if Algorithm 1 fails to find a valid solution.

7. On-Orbit Assembly Example

We consider an example of the large truss-based structure on-orbit assembly using the proposed approach for fuelless control of the servicing spacecraft motion. As described in Section 2, it is assumed that, initially, in orbit, there is a CC with a set of rods, installing a platform placed on the CC; the TS is to be assembled using rods and an SS with two manipulators. The structure to be assembled is the antenna-like construction presented in Figure 10.

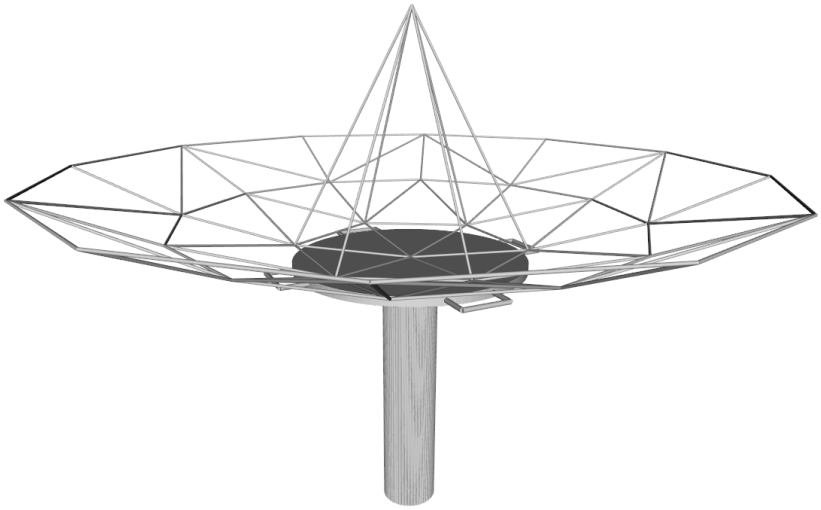

Figure 10. Large space truss structure to be assembled.

The main parameters of the considered system and parameters of the algorithms are provided in Table 2. The initial circular orbit height of the UB is 800 km, which corresponds to an orbital period of about 5700 s. It is assumed that the SS is initially attached to the CC. During the assembly process, the motion of the system is influenced by the central gravity field and by the repulsion and capturing of the SS. The effects of any orbital disturbances such as the second harmonic of Earth's gravity field, aerodynamic forces, solar pressure, etc., are neglected. Initially, the UB is stabilized in ORF; the axes of BRF coincide with ORF's axes.

Table 2. Main system parameters.

Variable	Value
The SS's mass	20 kg
The UB's initial mass	650 kg
Number of rods	78
Length of rods	5–10 m
Linear mass density of rods	1 kg/m
Maximum SS repulsion velocity v_0^{BRF}	0.05 m/s
$max\|\boldsymbol{\omega}_{UB}^{ORF}\|$	0.001 rad/s
$max\|\boldsymbol{r}_{UB}^{ORF}\|$	500 m
$max\|\boldsymbol{v}_{UB}^{ORF}\|$	0.1 m/s
Radius of collision avoidance zone around rods	30 cm
Manipulator capture radius	50 cm
Maximum motion time t_f^{max}	10^4 s

7.1. Acceptable Repulsion Velocity Restriction

For the proposed assembly method, it is the most important to estimate the required maximum value for the SS's repulsion velocity to perform the rod transfers. This value can be estimated using the simplified motion cases described above. In Equation (23), for the calculation of the initial guess for the repulsion velocity, the x- and z-components of repulsion velocity have same denominator. Furthermore, the same denominator is applied to the x- and z-components of repulsion velocity in Equation (18) for the planar motion case. Values of the denominator (23) for the x- and z-components depending on transfer time are represented in Figure 11. Transfer time regions' near-zero value of the denominator requires an extremely large repulsion velocity and should be avoided by choosing an appropriate transfer time. Additionally, the y-component denominator (23) is zero during one-half of the orbital period. Thus, transfer time regions with high denominator values should be chosen.

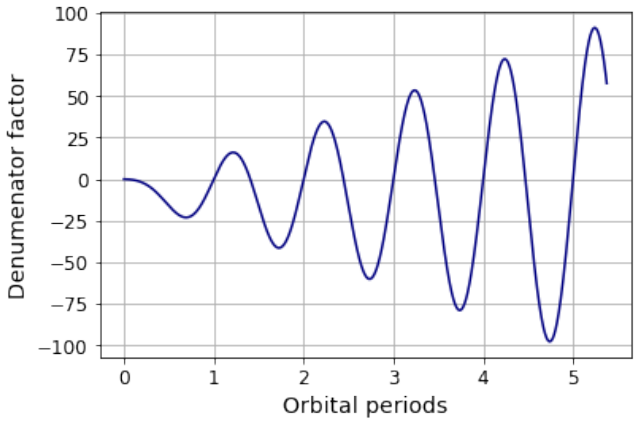

Figure 11. Repulsion velocity of x- and z-components' denominator in (23) depending on transfer time.

Examples of the required repulsion velocity values (23) and (18) according to simplified cases for randomly generated one hundred transfers between structure points are shown in Figures 12 and 13. Blue boxplots correspond to formulas (23), and yellow boxplots correspond to formulas (18). Half of the results are inside the box and the horizontal line is the median value of the required repulsion velocity. Figure 12 demonstrates the repulsion velocities' boxplots for transfers between points with a structure of an overall size of $L = 20$ m, which corresponds to the structure's overall size of the antenna-like structure

considered in this section. For comparison, Figure 13 presents the repulsion velocities' boxplots for the transfers with a structure of an overall size of $L = 100$ m. It can be noticed that the short transfer time when the denominator is small results in higher values of the repulsion velocities. In the case of a time transfer of 3000 s, the values of the repulsion velocities are also high because this is close to the half of the orbital period and close to the zero-value of the denominator for the y-component's velocity in (23). For the other cases of time transfer, the required repulsion velocity is less than the value of 5 cm/s for the structure with a characteristic size of $L = 20$ m, and 20 cm/s for $L = 100$ m.

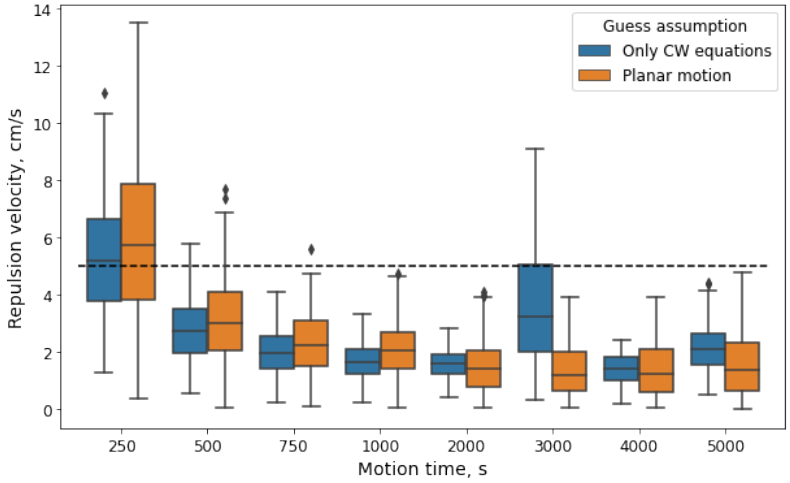

Figure 12. Repulsion velocity values at fixed motion time for randomly generated transfers between points of the structure with characteristic size $L = 20$ m.

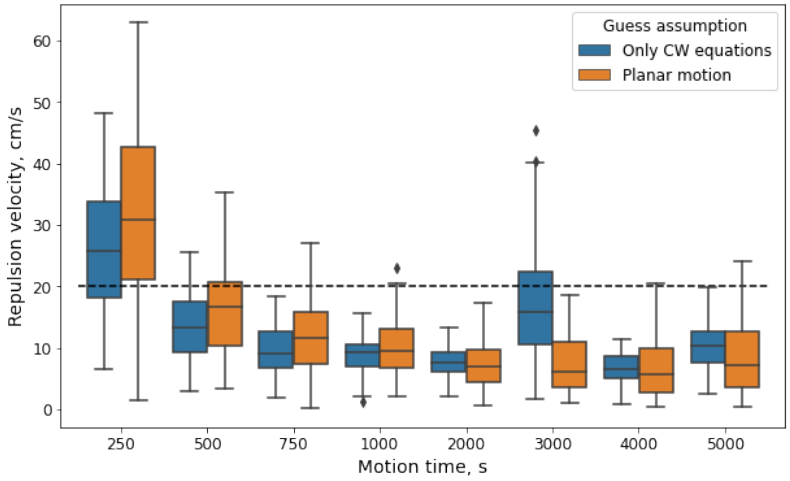

Figure 13. Repulsion velocity values at fixed motion time for randomly generated transfers between points of the structure with characteristic size $L = 100$ m.

Thus, in this example of space structure assembly, the repulsion velocity is restricted by the reasonable value of 5 cm/s, though, in practice, this restriction is the result of the choice of a particular SS's manipulators and its parameters.

7.2. Simulation of the Assembly Process

The assembly process consists of a sequence of predetermined transfers of the SS between the UB's points. Initially, the SS is located at the CC, it takes the rod, and then repulses from the UB using the manipulator. When the SS's trajectory is in the vicinity of the target point, the SS's manipulators capture the UB; then, the SS installs the rod to the

structure and repulses by manipulator to transfer to the initial point at the CC to take the next rod. Then, the cycle is repeated until the structure is fully assembled.

Figure 14 presents an example of the SS's position deviation from the target point during the SS's motion (top plot) and the values of the constrained-motion parameters (19) divided by their maximum values c_i/c_i^{max} (bottom plot). The vector of the constrained-motion parameters includes the value of the UB's angular velocity $\boldsymbol{\omega}_{UB}^{ORF}$, and the UB's center of mass's position $\boldsymbol{r}_{UB}^{ORF}$ and velocity $\boldsymbol{v}_{UB}^{ORF}$; their maximum values are provided in Table 2. In Figure 14, red vertical dashed lines indicates time points of the SS's repulsion and catching by the UB. The catching is performed when the SS's position deviation is less than the length of the manipulator capture radius of 0.5 m. The SS and the UB's free-flight motion takes place between the repulsion and catching points. As can be seen from Figure 14, at the time moments of the SS's repulsion from the UB and catching by the UB, the UB's angular and translational velocities change simultaneously according to (12) and (14). The change in the UB's angular velocity is caused by oscillations of the UB in the vicinity of the gravity-stable orientation.

The repulsion velocities for the presented transfers are found using the two algorithms described above of numerical search. Figure 15 presents an example of the convergence process of reducing the SS's final position deviation vs. the number of required iterations in the case where Algorithm 1 is used to solve the problem using an initial velocity guess calculated for simplified cases. Algorithm 1 stops when the $\Delta r(t)$ is less than the manipulator's capture radius of 0.5 m, or when the difference between the two values of the repulsion velocities $\left|\boldsymbol{v_0}^{i+1} - \boldsymbol{v_0}^{i}\right| < \varepsilon_{v_0}$ is less than $\varepsilon_{v_0} = 10^{-4}$ m/s. In most cases presented in Figure 15, Algorithm 1 successfully finds the repulsion velocity with $\Delta r(t) < 0.5$ m taking into account the collision avoidance aspect according to Approach 1 described in Section 6.1. However, in some cases, Algorithm 1 fails to find a solution as is shown by the red line in Figure 15: the $\Delta r(t)$ is more than the manipulator's capture radius and the repulsion velocity is converged. In that case, Algorithm 2 is used to solve the problem (21). An example of the convergence process of Algorithm 2 is presented in Figure 16. It requires many more iterations, though, since it uses the more complicated Approach 2 to take into account the collision avoidance with the structure, it finds solution to the transfer problem more steadily. It can be noted from Figure 16 that the position error decreases insignificantly from 10 to 45 iterations. It can be explained by the slow convergence rate of the trust region method in the area close to the violation of condition $g_i \geq 0$ (20) related to structure collision avoidance.

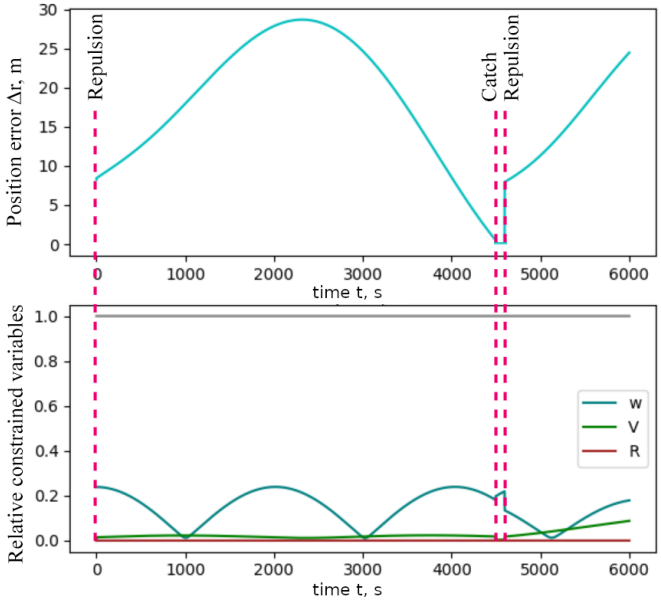

Figure 14. The SS's deviation from the target point $\Delta r(t)$ (**top**) and the relative values c_i/c_i^{max} of the constrained-motion parameters (19) (**bottom**) during the SS's motion.

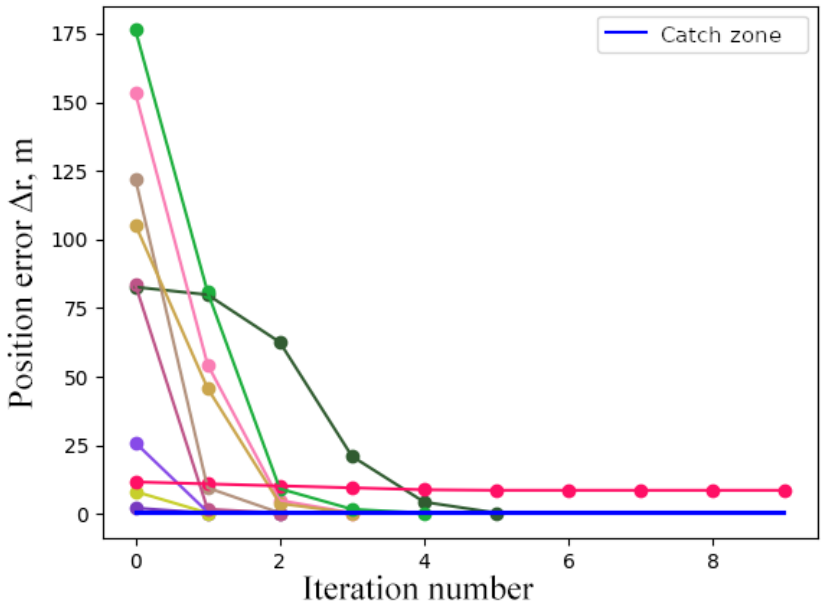

Figure 15. A set of examples of final position deviation during the numerical search by Algorithm 1. Each colored line corresponds to different example.

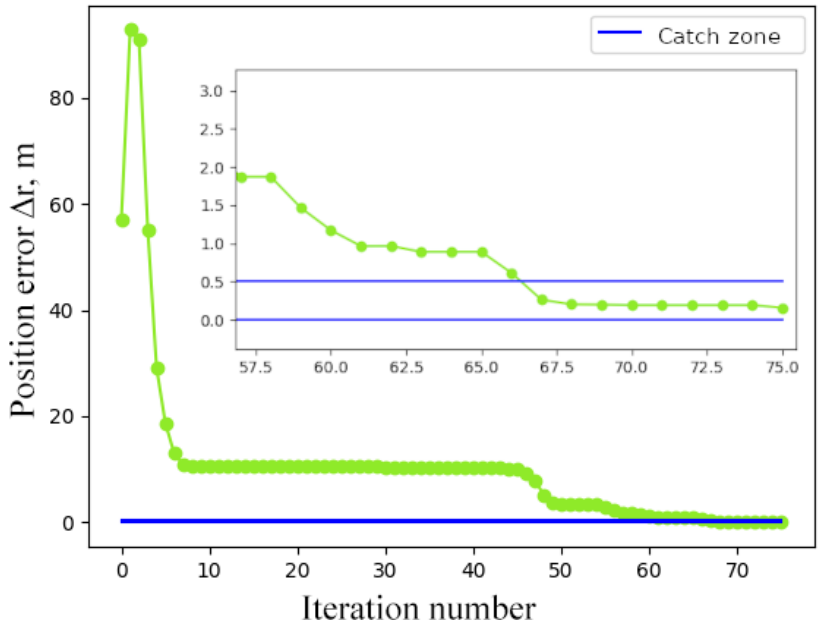

Figure 16. An example of final position deviation during the numerical search by Algorithm 2.

Figure 17 presents the SS's position deviation from the target points during several transfers. Furthermore, in Figure 18, the relative constrained-motion parameters during multiple transfers are shown. From Figure 18, it can be seen that the relative constrained values do not exceed the value of 1, so the relative constrained values are not violated. However, the SS's repulsion impulses and the change of the UB's mass distribution may lead to the significant deviation of the UB from the gravity-stabilized attitude and result in an increase of the angular velocity.

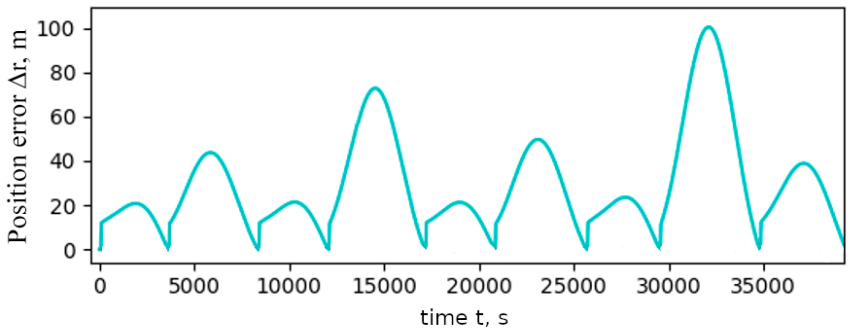

Figure 17. The SS's deviation from the target point $\Delta r(t)$ during multiple transfers.

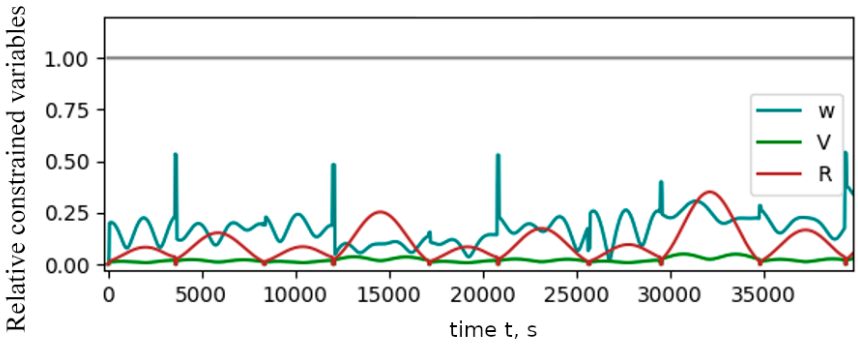

Figure 18. Relative values c_i/c_i^{max} of the constrained-motion parameters (19) during multiple transfers.

Intermediate assembly stages are shown in Figures 19 and 20. In these figures, the CC, the SS, trajectories of the SS, and a set of the installed rods are presented. In Figure 19, most of the rods are still inside the CC, and the symmetry axis of the cylindrical CC with a minimal inertia moment is almost aligned with the local vertical axis z of ORF. So, the UB's attitude is in the vicinity of the gravity-gradient stabilization equilibrium. After a while, the mass distribution is changed, and the attitude of the UB due to SS's repulsion is also changed significantly according to Figure 20.

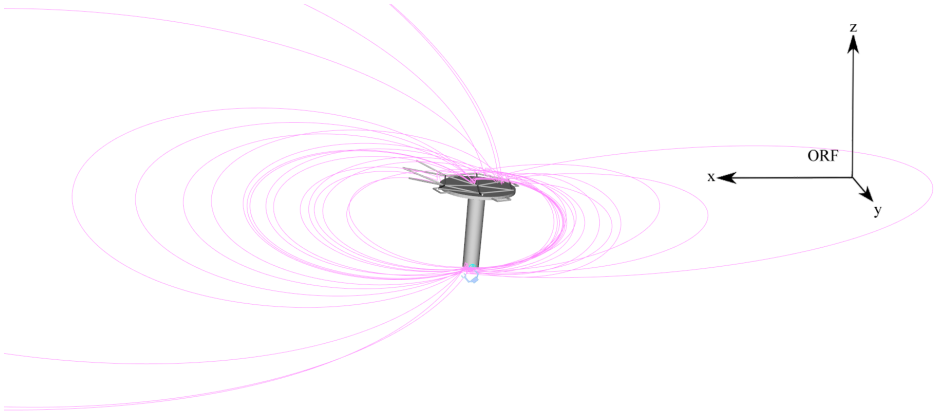

Figure 19. Intermediate stage of assembly: cargo container, servicing satellite, and its trajectories during the transfers.

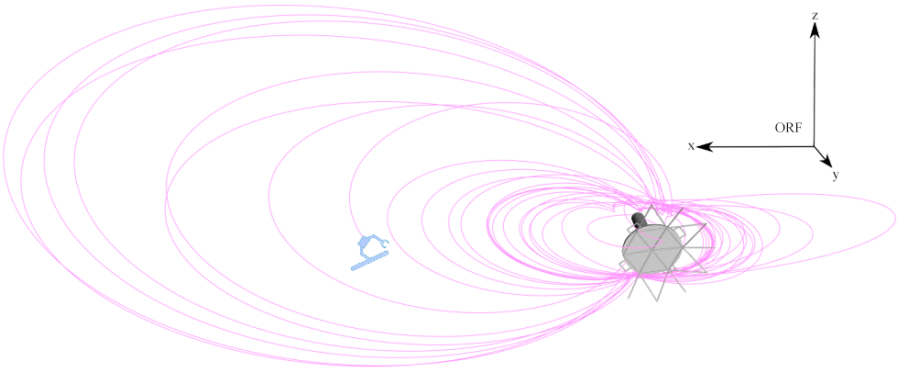

Figure 20. Demonstration of attitude change of the assembling structure.

Figure 21 shows the values of the calculated SS's repulsion velocities during the assembly process. It can be concluded that, due to slightly increasing UB's angular velocity, the maximal values of the SS's repulsion velocity also steadily increase, though they do not exceed the limit of 5 cm/s. It means that the estimations of the maximum repulsion velocity obtained using the simplified motion cases (see Figure 12) are valid for the considered example.

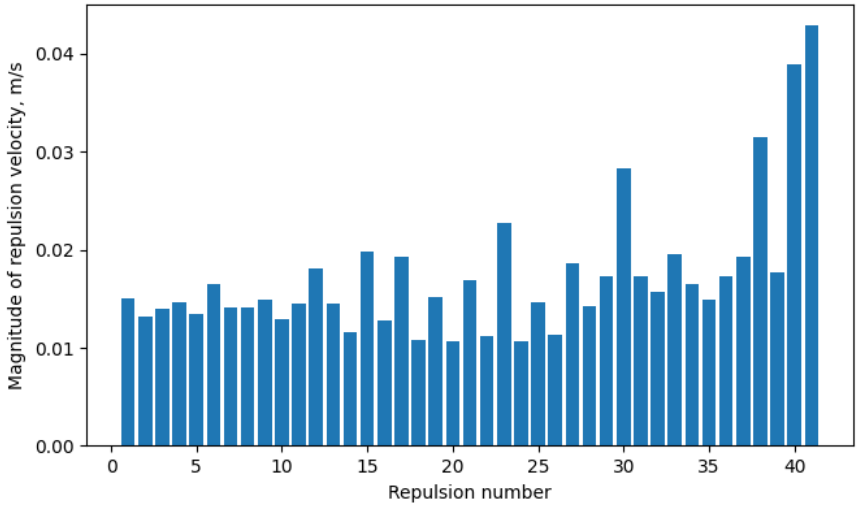

Figure 21. Repulsion velocity values during the space structure assembly.

8. Conclusions

This paper proposed a new approach to the problem of the space structure construction using the servicing spacecraft with two manipulators. With these manipulators, the servicing spacecraft is able to move between the structure points using repulsion and catching. In the case of planar motion, the boundary problem was solved analytically using simplifying assumptions. In the spatial motion case, the repulsive velocity was searched for using numerical minimization techniques, taking into account a set of restrictions on the motion parameters and considering collision avoidance of the servicing spacecraft with the space structure. A numerical example demonstrated the successful construction of the particular antenna-like truss structure. However, it should be noted that, in the case of a complex truss-based structure or at a high angular velocity of the structure, the acceptable repulsion velocity for the rod transfers could not be found in a feasible region of velocity vector. In this case, the servicing spacecraft would need to be equipped with onboard propulsion and the repulsion by manipulator can be considered as a means for reducing the fuel consumption. This case will be considered in further studies by the authors.

Author Contributions: Software, validation, and writing—original draft, V.O.; formal analysis, U.M.; methodology and project administration, M.O.; supervision, conceptualization and writing—review and editing, D.I. All authors have read and agreed to the published version of the manuscript.

Funding: This work was supported by the Moscow Center of Fundamental and Applied Mathematics, Agreement with the Ministry of Science and Higher Education of the Russian Federation, No. 075-15-2022-283.

Data Availability Statement: Data is contained within the article.

Conflicts of Interest: The authors declare no conflicts of interest.

Abbreviations

The following abbreviations are used in this manuscript:

IRF	Inertial reference frame
ORF	Orbital reference frame
BRF	Body reference frame
SRF	Structure reference frame
SS	Servicing spacecraft
TS	Truss structure
CC	Cargo container
UB	United body

References

1. Piskorz, D.; Jones, L.K. On-orbit assembly of space assets: A path to affordable and adaptable space infrastructure. *Aerosp. Corp.* **2018**, 1–10. Available online: https://aerospace.org/sites/default/files/2018-05/OnOrbitAssembly_0.pdf (accessed on 30 July 2024).
2. Davis, J.P.; Mayberry, J.P.; Penn, J.P. On-orbit servicing: Inspection repair refuel upgrade and assembly of satellites in space. *Aerosp. Corp.* **2019**, 1–14. Available online: https://aerospace.org/sites/default/files/2019-05/Davis-Mayberry-Penn_OOS_04242019.pdf (accessed on 30 July 2024).
3. Oegerle, W.R.; Purves, L.R.; Budinoff, J.G.; Moe, R.V.; Carnahan, T.M.; Evans, D.C.; Kim, C.K. Concept for a large scalable space telescope: In-space assembly. *Space Telesc. Instrum. I Opt. Infrared Millim.* **2006**, *6265*, 755–766.
4. Izzo, D.; Pettazzi, L.; Ayre, M. Mission Concept for Autonomous on Orbit Assembly of a Large Reflector in Space. In Proceedings of the 56th International Astronautical Congress, Fukuoka, Japan, 17–21 October 2005; IAC-05-D1.4.03.
5. Gralla, E.L.; De Weck, O.L. Strategies for on-orbit assembly of modular spacecraft. *J. Br. Interplanet. Soc.* **2007**, *60*, 219–227.
6. Sternberg, D.; Chodas, M.; Jewison, C.; Jones, M.; De Weck, O. Multidisciplinary system design optimization of on orbit satellite assembly architectures. In Proceedings of the 2015 IEEE Aerospace Conference, Big Sky, MT, USA, 7–14 March 2015.
7. McInnes, C.R. Distributed control of maneuvering vehicles for on-orbit assembly. *J. Guid. Control Dyn.* **1995**, *18*, 1204–1206. [CrossRef]
8. Izzo, D.; Pettazzi, L. Equilibrium shaping: Distributed motion planning for satellite swarm. In Proceedings of the 8th International Symposium on Artificial Intelligence, Robotics and Automation in space, Munich, Germany, 5–8 September 2005.
9. Underwood, C.; Pellegrino, S.; Lappas, V.J.; Bridges, C.P.; Baker, J. Using CubeSat/micro-satellite technology to demonstrate the Autonomous Assembly of a Reconfigurable Space Telescope (AAReST). *Acta Astronaut.* **2015**, *114*, 112–122. [CrossRef]
10. Cheng, Z.; Hou, X.; Zhang, X.; Zhou, L.; Guo, J.; Song, C. On-orbit assembly mission for the space solar power station. *Acta Astronaut.* **2016**, *129*, 299–308. [CrossRef]
11. On-Orbit Servicing, Assembly, and Manufacturing 2 (OSAM-2). Available online: https://www.nasa.gov/mission/on-orbit-servicing-assembly-and-manufacturing-2-osam-2/ (accessed on 2 November 2023).
12. Li, W.J.; Cheng, D.Y.; Liu, X.G.; Wang, Y.B.; Shi, W.H.; Tang, Z.X.; Gao, F.; Zeng, F.M.; Chai, H.Y.; Luo, W.B.; et al. On-orbit service (OOS) of spacecraft: A review of engineering developments. *Prog. Aerosp. Sci.* **2019**, *108*, 32–120. [CrossRef]
13. Akhloumadi, M.; Ivanov, D. Satellite Motion Control System Parameters on Performance of Space Debris Capturing. *Aerospace* **2020**, *7*, 160. [CrossRef]
14. Rutkovskii, V.Y.; Sukhanov, V.M.; Glumov, V.M. Motion equations and control of the free-flying space manipulator in the reconfiguration mode. *Autom. Remote Control* **2010**, *71*, 70–86. [CrossRef]
15. Glumov, V.M.; Krutova, I.N.; Sukhanov, V.M. Some features of powered gyrostabilization of a large space structure assembled in orbit. *Autom. Remote Control* **2018**, *79*, 524–534. [CrossRef]
16. Glumov, V.M.; Rutkovskii, V.Y.; Sukhanov, V.M. Formation of the control strategy for the large space structure assembled in orbit. *Autom. Remote Control* **2007**, *68*, 2113–2127. [CrossRef]

17. Uzo-Okoro, E.; Erkel, D.; Manandhar, P.; Dahl, M.; Kiley, E.; Cahoy, K.; De Weck, O.L. Optimization of On-Orbit Robotic Assembly of Small Satellites. In Proceedings of the Accelerating Space Commerce, Exploration, and New Discovery Conference, Las Vegas, NV, USA, 16–18 November 2020; American Institute of Aeronautics and Astronautics: Reston, VA, USA, 2020.
18. Pisculli, A.; Felicetti, L.; Gasbarri, P.; Palmerini, G.B.; Sabatini, M. A reaction-null/Jacobian transpose control strategy with gravity gradient compensation for on-orbit space manipulators. *Aerosp. Sci. Technol.* **2014**, *38*, 30–40. [CrossRef]
19. Palma, P.; Seweryn, K.; Rybus, T. Impedance control using selected compliant prismatic joint in a free-floating space manipulator. *Aerospace* **2022**, *9*, 406. [CrossRef]
20. Liu, J.; Zhao, P.; Chen, K.; Zhang, X.; Zhang, X. 1U-Sized Deployable Space Manipulator for Future On-Orbit Servicing, Assembly, and Manufacturing. *Space Sci. Technol.* **2022**, *2022*, 1–14. [CrossRef]
21. Hubert Delisle, M.; Christidi-Loumpasefski, O.-O.; Yalçın, B.C.; Li, X.; Olivares-Mendez, M.; Martinez, C. Hybrid-Compliant System for Soft Capture of Uncooperative Space Debris. *Appl. Sci.* **2023**, *13*, 7968. [CrossRef]
22. Magarotto, M.; Manente, M.; Pavarin, D. Electric Propulsion for CubeSats: A Review. In Proceedings of the 72nd International Astronautical Congress (IAC), Dubai, United Arab Emirates, 25 October 2021; IAC-21,C4,8-B4.5A,1,x64088.
23. Schäfer, F.; Montag, C.; Herdrich, G.; Laufer, R. Flight results of the PETRUS pulsed plasma thruster on the 3u CubeSat GreenCube. In Proceedings of the 73rd International Astronautical Congress (IAC), Paris, France, 18–22 September 2022; IAC-22,C4,8-B4.5A.
24. Borelli, G.; Gaias, G.; Nakajima, Y.; Colombo, C.; Capuano, V.; Saggiomo, F.; Leccese, G.; Natalucci, S. Mission analysis and guidance and control for the SpEye inspection CubeSat. *Acta Astronaut.* **2024**, *220*, 75–87. [CrossRef]
25. Ivanov, D.; Shestakov, S.; Ovchinnikov, M. Satellite formation flying control by mass exchange. *Acta Astronaut.* **2014**, *102*, 392–401.
26. Clohessy, W.H.; Wiltshire, R.S. Terminal Guidance System for Satellite Rendezvous. *J. Aerosp. Sci.* **1960**, *27*, 653–658. [CrossRef]
27. Sazonov, V.V.; Barbashova, T.F. *Gravitational Orientation of Artificial Earth Satellites: A Special Course*; CURS: Moscow, Russia, 2023; pp. 1–144.
28. Badawy, A.; McInnes, C.R. On-orbit assembly using superquadric potential fields. *J. Guid. Control Dyn.* **2008**, *31*, 30–43. [CrossRef]
29. Nesterov, Y.E. *Convex Optimiation Methods (Metody Vypukloj Optimizacii)*; ICNMO Publishing House: Moscow, Russia, 2010; pp. 1–281.
30. Fletcher, R. *Practical Methods of Optimization*; John Wiley & Sons: New York, NY, USA, 1987; pp. 1–455.